




Article

Estimation of Tree Vitality Reduced by Pine Needle Disease Using Multispectral Drone Images

Langning Huo ^{1,*} , Iryna Matsiakh ^{2,3}, Jonas Bohlin ¹  and Michelle Cleary ² 

¹ Department of Forest Resource Management, Swedish University of Agriculture Sciences, 901 83 Umea, Sweden; jonas.bohlin@slu.se

² Southern Swedish Forest Research Centre, Swedish University of Agricultural Sciences, 230 53 Alnarp, Sweden; iryna.matsiakh@slu.se (I.M.); michelle.cleary@slu.se (M.C.)

³ Institute of Forestry and Park Gardening, Ukrainian National Forestry University, 79057 Lviv, Ukraine

* Correspondence: langning.huo@slu.se

Abstract: Multispectral imagery from unmanned aerial vehicles (UAVs) can provide high-resolution data to map tree mortality caused by pests or diseases. Although many studies have investigated UAV-imagery-based methods to detect trees under acute stress followed by tree mortality, few have tested the feasibility and accuracy of detecting trees under chronic stress. This study aims to develop methods and test how well UAV-based multispectral imagery can detect pine needle disease long before tree mortality. Multispectral images were acquired four times through the growing season in an area with pine trees infected by needle pathogens. Vegetation indices (VIs) were used to quantify the decline in vitality, which was verified by tree needle retention (%) estimated from the ground. Results showed that several VIs had strong correlations with the needle retention level and were used to identify severely defoliated trees (<75% needle retention) with 0.71 overall classification accuracy, while the accuracy of detecting slightly defoliated trees (>75% needle retention) was very low. The results from one study area also implied more defoliation observed from the UAV (top view) than from the ground (bottom view). We conclude that using UAV-based multispectral imagery can efficiently identify severely defoliated trees caused by needle-cast pathogens, thus assisting forest health monitoring.

Keywords: unmanned aerial vehicle (UAV); multispectral imagery; pine needle disease; *Lophodermium*; forest monitoring; surveillance



Academic Editor: Ruyin Cao

Received: 21 November 2024

Revised: 23 December 2024

Accepted: 25 December 2024

Published: 14 January 2025

Citation: Huo, L.; Matsiakh, I.; Bohlin, J.; Cleary, M. Estimation of Tree Vitality Reduced by Pine Needle Disease Using Multispectral Drone Images. *Remote Sens.* **2025**, *17*, 271. <https://doi.org/10.3390/rs17020271>

Copyright: © 2025 by the authors. Licensee MDPI, Basel, Switzerland. This article is an open access article distributed under the terms and conditions of the Creative Commons Attribution (CC BY) license (<https://creativecommons.org/licenses/by/4.0/>).

1. Introduction

Coniferous forests that include *Pinus* species are a valuable natural resource that plays a crucial role in carbon sequestration, providing habitat to support biodiversity and the provisioning of other ecosystem services. In Fennoscandian boreal forests, Scots pine (*Pinus sylvestris*) is a dominant and economically important species, e.g., in Sweden, comprising about 39% of the standing forest volume (SLU, 2024), and has a wide ecological amplitude that is able to tolerate a range of soil conditions (Krakau et al. 2013). Despite being an isohydric species [1], Scots pine can be very sensitive to drought [2–4]. In addition, Scots pine is susceptible to several Ascomycota pathogens that cause needle blight or needle-cast diseases which reduce the photosynthetic capacity of needles, leading to premature defoliation, loss of tree vitality, and in severe cases, tree death. Examples of this include *Dothistroma septosporum*, *Lophodermella sulcigena* and species of *Lophodermium* including *L. pinastri*, *L. seditiosum* and *L. conigenum* [5–8]. Aside from the negative implications on tree growth that are expected with the increased frequency and severity of drought events,

climate change will increase the susceptibility of trees to biotic agents, including fungal pathogens which can accelerate the mortality of already weakened trees [9–11]. Moreover, changes in temperature, precipitation and humidity patterns can make conditions more favorable for pathogens development, whereby even latent infections by fungi considered to be endophytes can become opportunistic and cause disease on the host plant [12,13].

The traditional surveillance of forests using ground-based surveys is a valuable strategy to account for current and periodic forest health conditions and can guide disease management approaches to reduce potential losses in productivity. However, such surveys are extremely laborious, costly, logistically challenging and only feasible at a small scale (i.e., plot level). In addition, ground surveys based on visual assessments alone can be influenced by human bias and potentially lead to inaccurate estimations of disease symptoms (e.g., foliar discoloration) and the degree of defoliation and therefore skew estimates of severity and spatial distribution of damage. Remote sensing technologies, including the use of unmanned aerial vehicles (UAVs) [14], are emerging as a valuable tool for monitoring forest health conditions that can alleviate the human bias and uncertainty expected of in situ surveys and allow for increased operational flexibility to provide coverage over large remote or inaccessible areas. High spatial and temporal resolution data can be captured from sensors based on subtle changes in the pigmentation composition of foliage (e.g., chlorophyll and carotenoid) resulting from reduced photosynthesis activity which may not be visible to the human eye [15–17]. These spectral or structural features associated with responses of trees to abiotic- or biotic-induced stress can also be detected during the early stages of infection, which is often critical timing for making informed decisions for disease management to possibly curb disease outbreaks.

Nevertheless, different stress agents can cause different degrees of damage in trees, and therefore, using remote sensing to identify damage can be easy or challenging, depending on the stress agents involved. Some stress agents can cause acute stress and mortality within one growing season, such as the wood-boring pest European spruce bark beetle (*Ips typographus* L.) and pine wilt disease (PWD) caused by nematodes [18]. When trees experience such acute stress and stop physiological activities, their spectral signature can be used to identify them before their symptoms become visible to human eyes [17,19]. Other stress agents can cause chronic tree physiological reactions and symptoms, such as drought, root rot caused by fungi or oomycetes, and needle-cast or blight diseases caused by various fungal pathogens. Due to the limited physiological reactions and symptoms to such chronic stress, some studies have shown it to be challenging to identify chronically stressed trees with high accuracy [20]. A systematic review identified 99 publications using UAV-based sensors on tree health monitoring published between 2012 and 2021. Only 5.6% and 8.0% of the publications investigated stress caused by drought and fungal pathogens, respectively [14]. Currently, there is a lack of research on detecting chronic stress using UAV-based methods, and the limited number of studies has shown that it is challenging to achieve high accuracy. Therefore, more efforts are needed to investigate and develop methodologies for chronic stress detection. In 2021, a local outbreak of pine needle disease was reported in mid-rotation Scots pine stands in southeastern Sweden. Reconnaissance surveys indicated that trees exhibited both recent and prolonged exposure to infection by one or more needle-cast pathogens, causing the discoloration and premature defoliation of needle cohorts in the upper and lower tree crown (Matsiakh et al. manuscript in preparation). The objective of this study was to (1) develop suitable methods for data acquisition and analysis using multispectral UAV images for detecting pine trees that are physiologically stressed as a result of pine needle-cast disease and (2) test the sensitivity of spectral signatures for indicating the degree of damage based on the amount of crown

defoliation and the early-onset physiological stress caused by needle disease while in a pre-symptomatic phase.

2. Materials and Methods

2.1. Study Area and Field Observations

The study site was located near Nybro in Kalmar county, southeastern Sweden (latitude 56.46274°N, longitude 15.75898°E) (Figure 1). The site is approximately 110 m above sea level and comprised of predominantly Scots pine mixed with Norway spruce. The site experiences a temperate climate (total annual rainfall = 628 mm, mean annual temperature = 6.5 °C) and mesic soils. Two stands in the production forest were surveyed to estimate the incidence and severity of disease. Trees in Stand 1 were approximately 70 years old and in Stand 2 were 45 years old; the site index for both sites is T26. Nine and six plots with a 10 m radius were established in Stands 1 and 2, respectively (Table 1), and the inventory was carried out in June. The amount of remaining needles of each tree was estimated per upper and lower half of the tree crown as 100%, 75% and 50%, and then averaged to give an overall severity rating per tree (Figure 2).

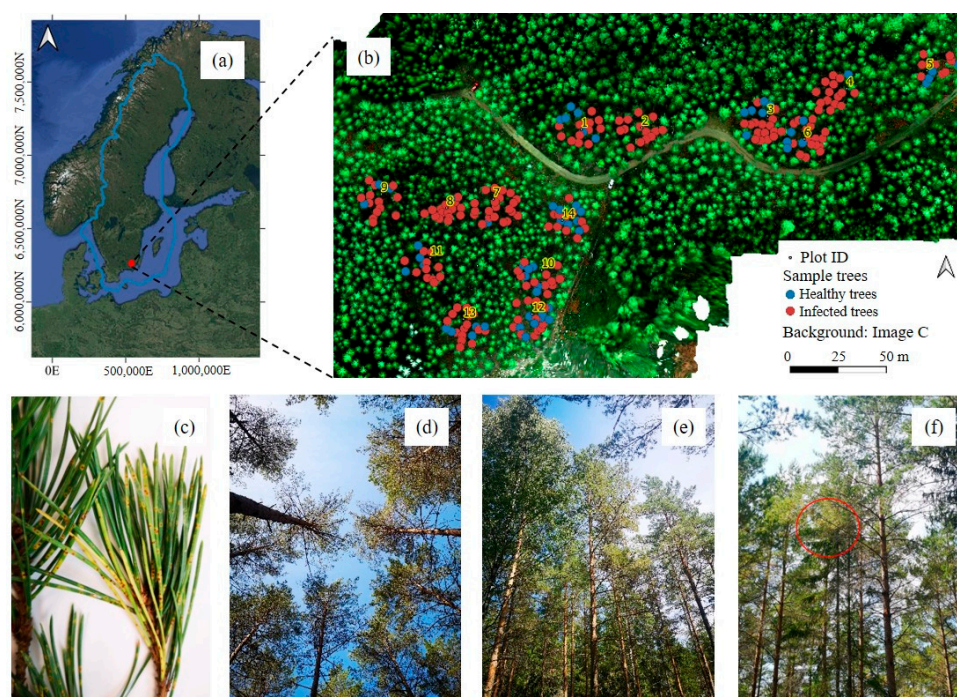


Figure 1. Study area located in southern Sweden (a), plot and tree locations (b), symptomatic needles showing chlorosis and brown spots caused by fungal pathogens (c), and photos showing variable crown symptoms and defoliation of mature Scots pine trees in May (d), June (e), and August (f); red circle denotes symptomatic branches. Plots 1–6 were in Stand No. 2 and Plots 9–14 were in Stand No. 1.

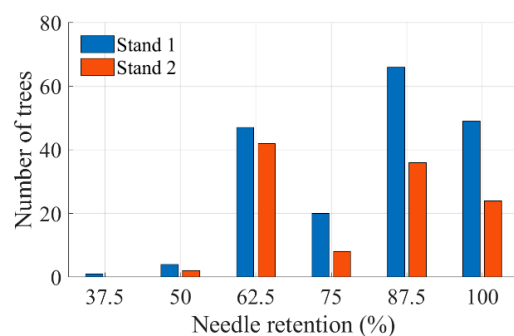


Figure 2. Distribution of needle retention (%) based on disease severity scoring of trees inventoried from the fieldwork.

Table 1. Stand and plot info.

Stand No.	Plot No.	Number of Trees with Location Info	Mean DBH (cm)	Mean Height (m)	Number of Healthy Trees	Number of Infested Trees
1	1	22	18.3	15.6	1	21
	2	16	20.4	16.6	1	15
	3	16	22.1	17.2	3	13
	4	19	18.1	15.9	7	12
	6	15	18.8	15.0	4	11
	7	21	17.1	15.5	8	13
	8	20	19.9	16.5	5	15
	9	20	19.0	15.1	8	12
	Sum/Average	149	17.8	15.1	37	112
2	1	18	25.3	18.0	6	12
	2	14	26.2	18.3	0	14
	3	22	24.7	17.9	6	16
	4	16	25.5	19.6	1	15
	5	13	29.8	22.5	4	9
	6	21	23.7	18.4	5	16
	Sum/Average	104	25.2	18.8	22	82
Total/Average	253	20.6	16.5	59	194	

2.2. Drone Image Acquisition and Preprocessing

Drone images were acquired four times (Table 2) from the study area using a MAIA S2 multispectral camera (SAL Engineering Srl, Russi, Italy, and Eoptis Srl, Trento, Italy) mounted on a DJI M210 RTK drone (SZ DJI Technology Co., Ltd., Shenzhen, China, Figure 3). The camera had nine spectral bands with wavelengths similar to those of images from the satellite Sentinel-2 (Table 3). The drone flew 120 m above ground with 80% forward and side overlap, generating a nominal ground sampling distance (GSD) of 6 cm. Raw images from MAIA camera were post-processed with the MAIA image-processing software (MAIA-1.4), including geometric correction, co-registration of each band, radiometric correction of the border effects, and radiometric correction using data from the MAIA Incident Light Sensor (ILS). The post-processed images (Figure 4a) were used to generate orthomosaic images (Figure 4b) using Agisoft Metashape Professional (Version 1.7.2, Copyright 2021 Agisoft LLC., St. Petersburg, Russia), including aligning photos, optimizing alignment, building a dense cloud, building digital surface models (DSMs), and building orthomosaics. The orthomosaic images were radiometrically transformed to reflectance (Figure 4c) using the known reflectance of the reference panels (1 m × 1 m). The four orthomosaic images were manually georeferenced with each other. In the following sections, the four orthomosaic images acquired at the four times were denoted as Images T1, T2, T3, and T4.

Table 2. Image number and acquired conditions.

Image	Acquired Time	Illumination Condition	Solar Elevation
T1	30 June 2022 13:15	Sunny	54.4
T2	31 August 2022 10:05	Sunny	36.9
T3	23 September 2022 11:12	Cloudy	32.7
T4	23 September 2022 09:55	Sunny	28.5

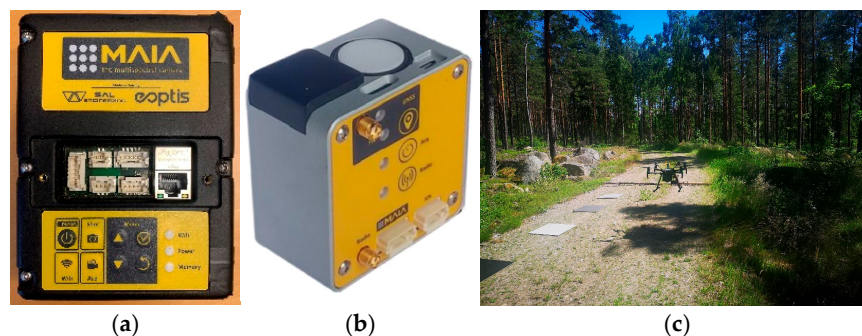


Figure 3. The MAIA camera (a), MAIA ILS (b), DJI Matrice 210 RTK drone, and the radiometric reference targets by the sampling plots (c).

Table 3. Summary of the MAIA S2 multispectral camera specifications.

Band no.	Color	Center Wavelength (nm)	Bandwidth (nm)
1	Violet	443	20
2	Blue	490	65
3	Green	560	35
4	Red	665	30
5	Red-edge 1	705	15
6	Red-edge 2	740	15
7	Red-edge 3	783	20
8	NIR 1	842	115
9	NIR 2	865	20

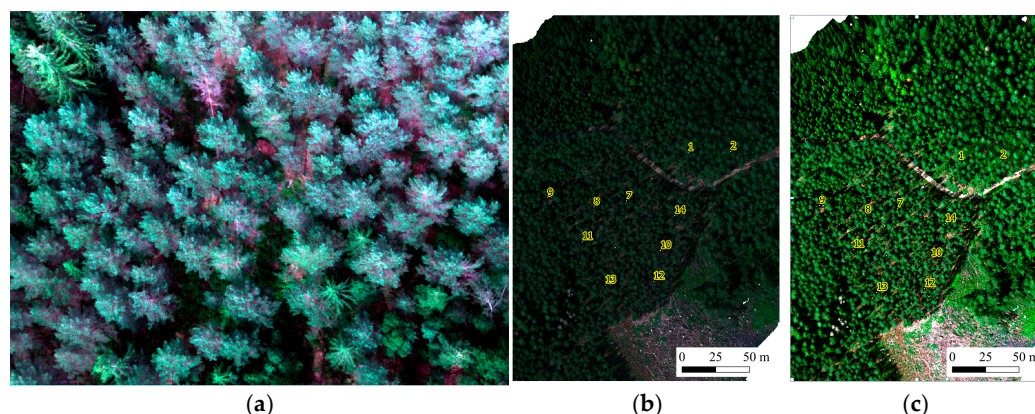


Figure 4. A post-processed MAIA image from June (a), and an orthomosaic image before (b) and after (c) radiometric correction using the radiometric reference targets. The images are illustrated with the red (665 nm), green (560 nm), and blue (490 nm) bands. The numbers in (b,c) are plot numbers.

2.3. Image Segmentation and Crown Spectrum Calculation

We used marker-controlled watershed segmentation presented by [21] to obtain the crown images of individual trees. The segmentation was first conducted on the green-band image, and the same mask was used for all the other bands. First, the images were smoothed by a Gaussian filter, and the local maxima were obtained as the tree tops and used as the markers for the watershed segmentation (Figure 5a). Then, the segmentation (Figure 5b) was conducted using the SegmentTrees tool in the Lidar Toolbox in Matlab (R2021b, MathWorks, Inc., Natick, MA, USA). Meanwhile, the pixels of the forest floor were masked out by calculating the Normalized Green-Red Difference Index (NGRDI, Table 4, Index 7, Figure 5b) from smoothed images and excluding the pixels with $NGRDI < 0.15$ (selected by visual evaluation of the masking results). Forest gaps with dark pixels were masked out by the reflectance of the green band < 0.05 [21]. The tree tops obtained from the

images were then matched with tree locations measured from the field, and the inventoried health status and needle retention levels were linked to the crown segments (Figure 5b). Crown segments were obtained (Figure 5c), and this study also tested the effective radius of crown segments on estimating the tree vitality (Figure 5d). Spectral reflectance was averaged from pixels within 0.25 m, 0.5 m, 0.75 m, and up to 2 m radius of a tree top (brightest pixel in the green band), respectively, and the averaged spectral reflectance was used to classify healthy and infected trees with comparison between different radii.

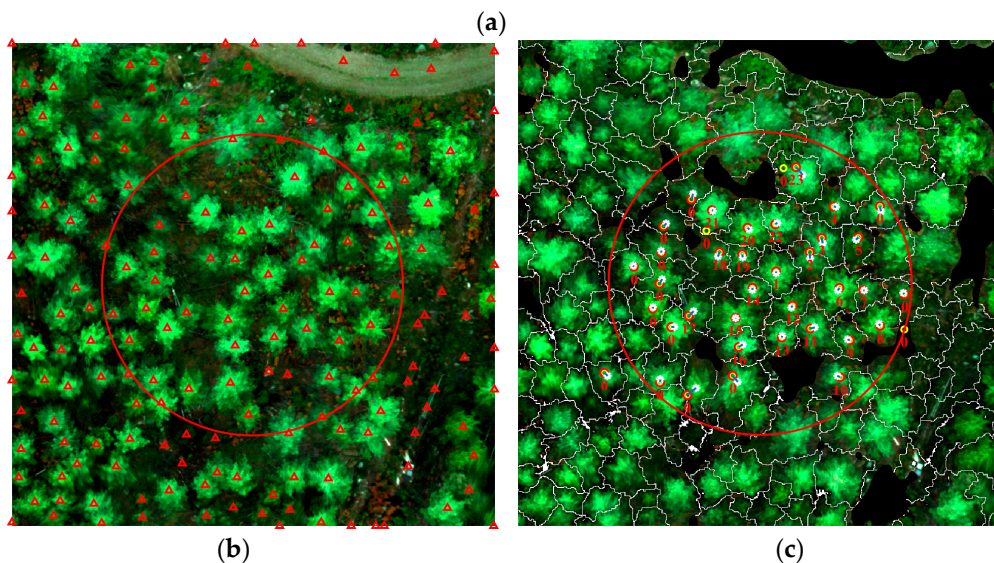
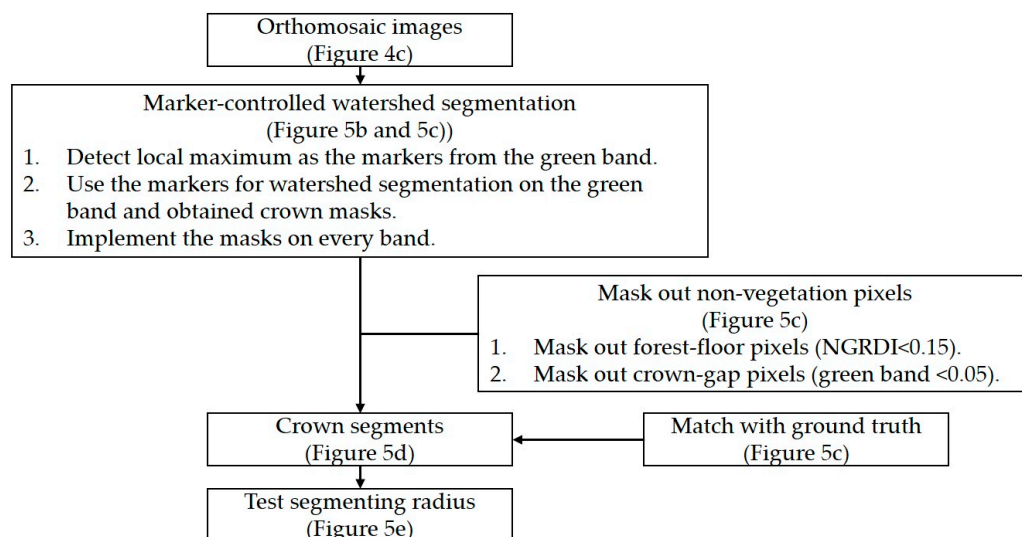


Figure 5. Cont.

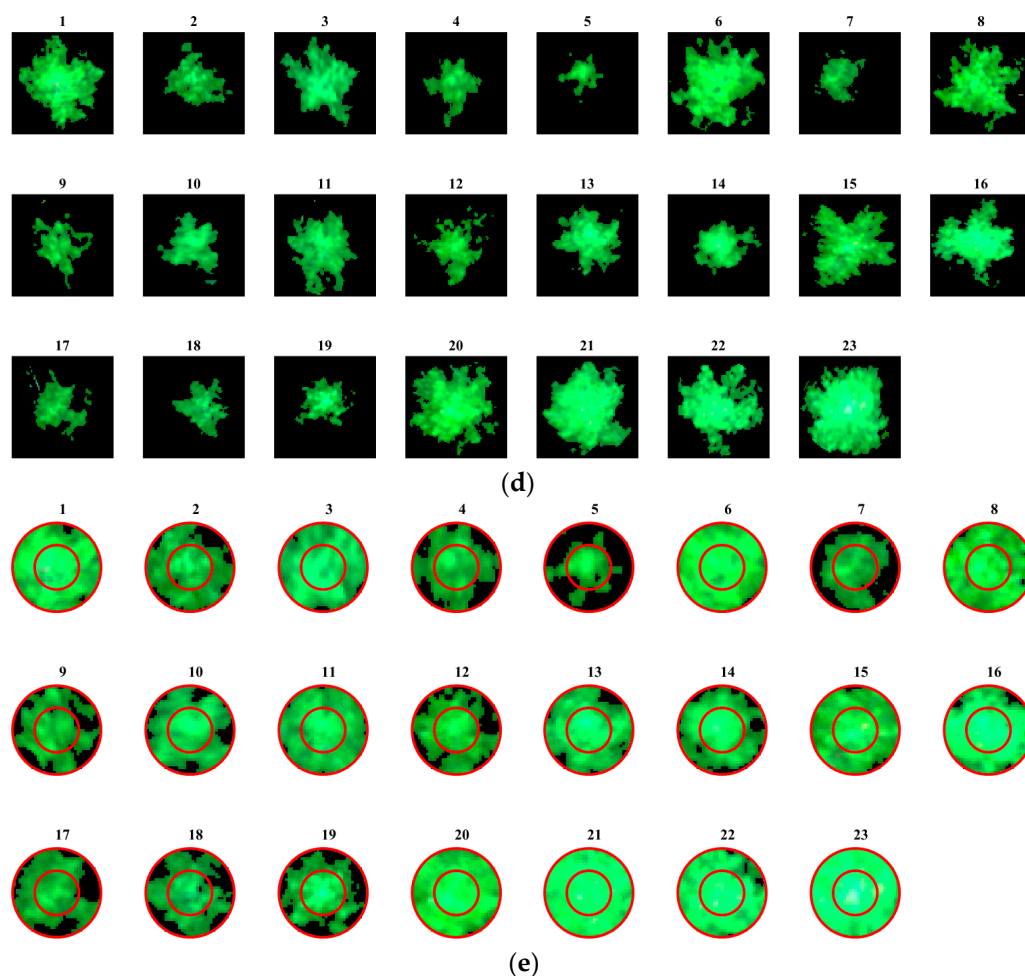


Figure 5. Segmentation of individual tree crowns from Image C at Stand 1 Plot 7. (a) A flowchart of the segmentation. (b) A true-color image covers 48×48 m area with the red circle marking the plot area with 15 m radius and red triangles marking the local maximum being the markers for the segmentation. (c) A true-color image covers 48×48 m area with the red circle marking the plot area with 15 m radius, white * and red dots marking the paired tree locations from the image and the field inventory, and yellow dots marking the tree locations inventoried from the fieldwork but missing from the image. The forest floor areas were masked from the background image, showing black. (d) Segments of individual tree crowns from the plot image. (e) Segments of individual tree crowns showing pixels within 1 m and 0.5 m radius (marked as red lines) to the center pixel.

2.4. Vegetation Indices and Estimation of Tree Vitality

After obtaining the average reflectance from crown segments, we first presented the spectral signatures of trees with different health statuses and tested the bands with significant differences between the following tree groups in different images:

- Group A: healthy trees;
- Group B: infected trees with needle retention $\geq 75\%$;
- Group C: infected trees with needle retention $< 75\%$.

The significance was tested between (1) Group A and Group B + C, and (2) Groups B and C, using a two-sided Wilcoxon rank sum test, which hypothesizes samples from continuous distributions with equal medians against the alternative that they are not. Fourteen vegetation indices (IVs, Table 4) were calculated and selected to estimate the health status. Linear Discriminant Analysis (LDA) was used to evaluate and compare the capacity of each VI to discriminate trees with different health statuses. LDA models the difference between the classes of data, and thus, the classification accuracy can indicate

how well each VI of damaged trees separates from healthy trees [17,21–23]. Four models were tested in the study to present the separability of those groups:

- Model I classified Group A vs. B + C;
- Model II classified Group A vs. B vs. C;
- Model III classified Group A vs. C;
- Model IV classified Group B vs. C.

In each model, samples were randomly selected to balance the sample size from each group, and classification accuracy, i.e., the number of correctly classified samples in proportion to all samples, was averaged by 20 times of random sample selection. Overall accuracy was calculated as the ratio between correctly classified samples and all samples. Results from Stands 1 and 2 were presented separately because of the potential difference between stands.

In addition, the classification results were further validated based on the VIs distribution. For example, if the VIs indicated infected trees with higher vitality than healthy trees, the classification was determined as invalidated, as LDA can only present the separability between several groups without testing whether the distributions were reasonable.

Table 4. Details of the vegetation indices (VIs) used.

No.	Abbr.	Name	Definition for MAIA S2/Sentinel-2 Bands (https://www.indexdatabase.de/ accessed on 30 November 2023)	References
1	REIP	Red-edge inflection point (guyot)	$700 + \left(\frac{(Red+Red_edge3) - Red_edge1}{Red_edge2 - Red_edge1} \right) \times 40$	[24]
2	MR-DSWI1	Multiple Ratio Disease–Water Stress Index 1	$\frac{Red_edge1}{Green} \times \frac{Red_edge1}{Red_edge3}$	[21]
3	MR-DSWI2	Multiple Ratio Disease–Water Stress Index 2	$\frac{Red_edge1}{Green} \times \frac{Red_edge1}{Red_edge3} \times \frac{NIR2}{Red_edge3}$	[21]
4	MR-DSWI3	Multiple Ratio Disease–Water Stress Index 3	$\frac{Red_edge1}{Green} \times \frac{Red_edge1}{Red_edge3} \times \frac{Red}{Green}$	[21]
5	MR-DSWI4	Multiple Ratio Disease–Water Stress Index 4	$\frac{Red_edge1}{Green} \times \frac{Red_edge1}{Red_edge3} \times \frac{NIR2}{Red_edge3} \times \frac{Red}{Green}$	[21]
6	NDRE2	Normalized Difference Red-edge Index 2	$\frac{Red_edge3 - Red_edge1}{Red_edge3 + Red_edge1}$	[25]
7	NGRDI	Normalized Green–Red Difference Index	$\frac{Green - Red}{Green + Red}$	[26]
8	NDVI	Normalized Difference Vegetation Index	$\frac{NIR2 - Red}{NIR2 + Red}$	[27]
9	GLI	Green Leaf Index	$\frac{(Green - Red) + (Green - Blue)}{(Green + Red) + (Green + Blue)}$	[28]
10	PBI	Plant Biochemical Index	$\frac{NIR2}{Green}$	[29]
11	GNDVI	Green Normalized Difference Vegetation Index	$\frac{NIR2 - Green}{NIR2 + Green}$	[30]
12	CIG	Chlorophyll Index Green	$\frac{NIR2}{Green} - 1$	[31]
13	CVI	Chlorophyll Vegetation Index	$\frac{NIR2 \times Red_edge1}{Green \times Green}$	[32]
14	NDRE3	Normalized Difference Red-edge Index 3	$\frac{NIR2 - Red_edge3}{NIR2 + Red_edge3}$	[33]

3. Results

3.1. Crown Segmentation

After crown segmentation and matching with field data, 123 trees out of 149 trees were successfully segmented from all four images in Stand 1 and 99 out of 104 trees from Stand 2 (Table 5). The segmentation success rates were 90%, 89%, 94%, and 90%, respectively, using Images T1, T2, T3, and T4. Undersegmentation occurred in trees with small crowns

or when two tree crowns were close to each other. The success rate was higher in Image T3, which was acquired under diffused light conditions, while the other images were acquired under direct light with shadows and bright forest floor in the images, thus influencing the watershed segmentation. Figure 6 shows the distribution of needle retention in Stands 1 and 2.

Table 5. Number of trees segmented from images.

Stand No.	Plot No.	Number of Trees Inventoried			Number of Trees Segmented from the Images						
		Healthy	Infected	All	T1	T2	T3	T4	All	Healthy	Infected
1	1	1	21	22	19	17	22	20	15	1	14
	2	1	15	16	14	16	16	16	14	0	14
	3	3	13	16	14	15	16	16	14	2	12
	4	7	12	19	18	18	19	19	18	6	12
	6	4	11	15	13	15	15	15	13	3	10
	7	8	13	21	20	19	20	18	15	4	11
	8	5	15	20	20	19	19	19	17	4	13
	9	8	12	20	20	19	19	18	17	7	10
	Sum	37	112	149	137	138	147	141	123	27	96
2	1	6	12	18	17	17	18	17	17	5	12
	2	0	14	14	14	14	14	14	14	0	14
	3	6	16	22	22	21	22	22	21	6	15
	4	1	15	16	16	16	16	15	15	1	14
	5	4	9	13	13	13	13	12	12	3	9
	6	5	16	21	21	20	21	21	20	5	15
Sum	22	82	104	103	101	104	101	99	20	79	
Total		16.5	59	268	240	239	251	242	222	47	175

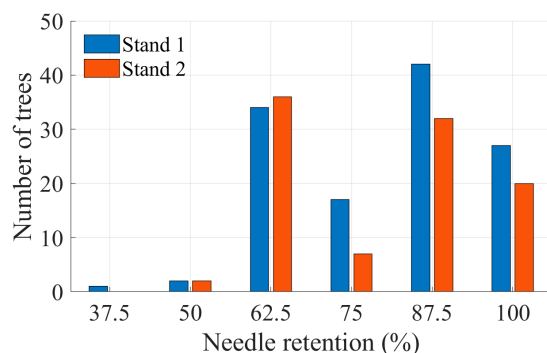


Figure 6. Distribution of the needle retention based on disease severity scoring in two stands from the trees with successfully segmented crown images.

3.2. Spectral Signatures and Significant Tests

The spectral signatures of different tree groups from different images and stands are presented in Figure 7. When a tree becomes infected and reduces vitality, the chlorophyll concentration usually decreases, causing decreases in the reflectance of Bands 1–5 while increasing in Bands 6–9. In this study, we assumed healthy trees to have higher vitality and thus higher chlorophyll concentration than infected trees, and so did the infected trees with needle retention $\geq 75\%$ compared to ones with needle retention $< 75\%$. In Stand 1, Bands 1–4 from infected trees had significantly higher reflectances than healthy trees in Images T1 and T3, while no significant differences were observed between infected trees with different needle retention levels (Figure 7a1,a2). Significant differences were also found in Image T4 in Bands 6–9. However, the variations of those bands within groups in Image T4 were also large. In Stand 2, many bands from healthy and infected trees

significantly differed in Images T3 and T4. However, the reflectances were opposite to what was assumed, indicating that healthy trees were more stressed or defoliated than the infected trees. When comparing infected trees with different needle retention levels in Stand 2, Bands 1–4 showed significantly higher reflectances among trees with more severe defoliation, matching our assumption that infected trees with lower needle retention were more stressed and had lower vitality.

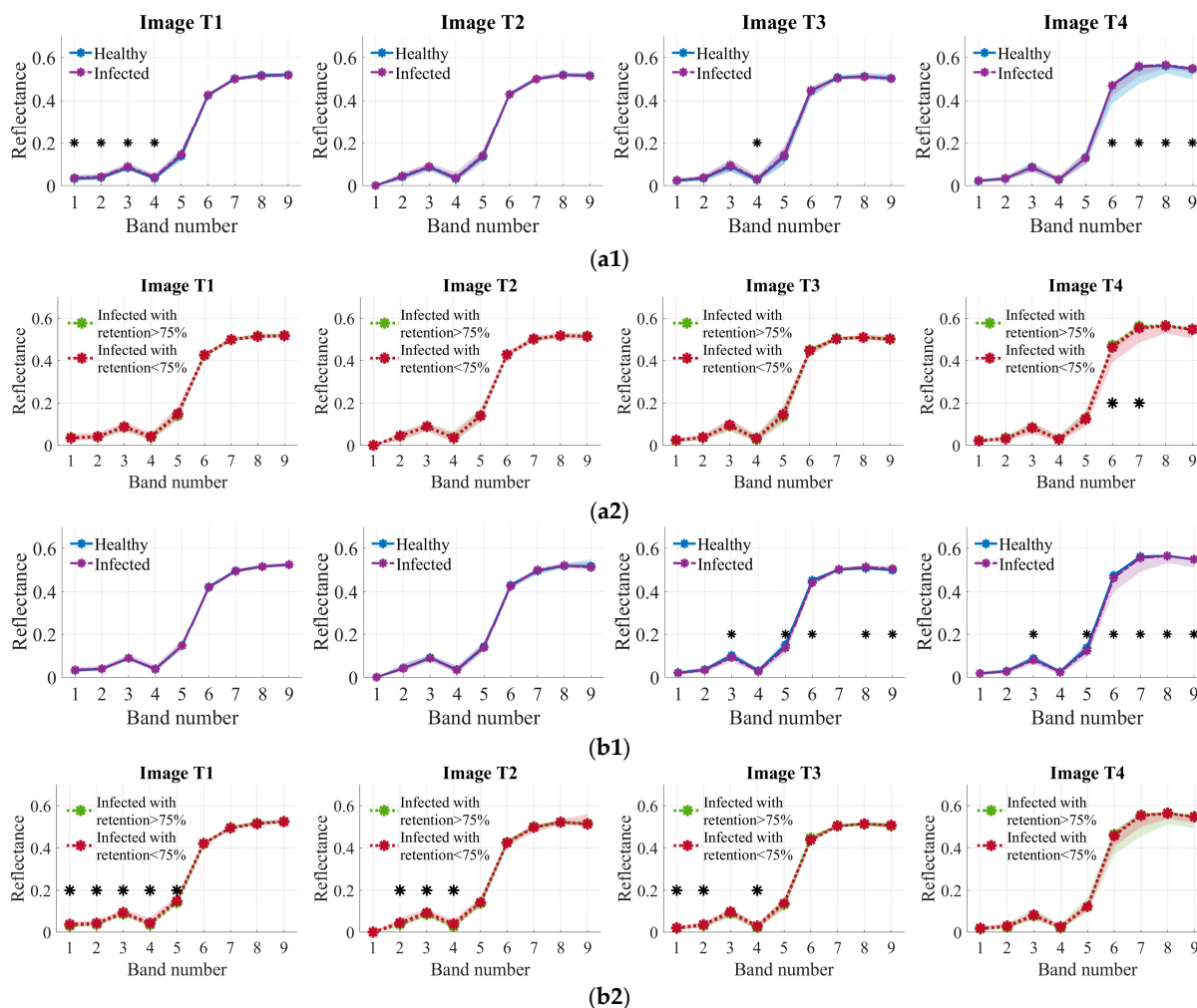
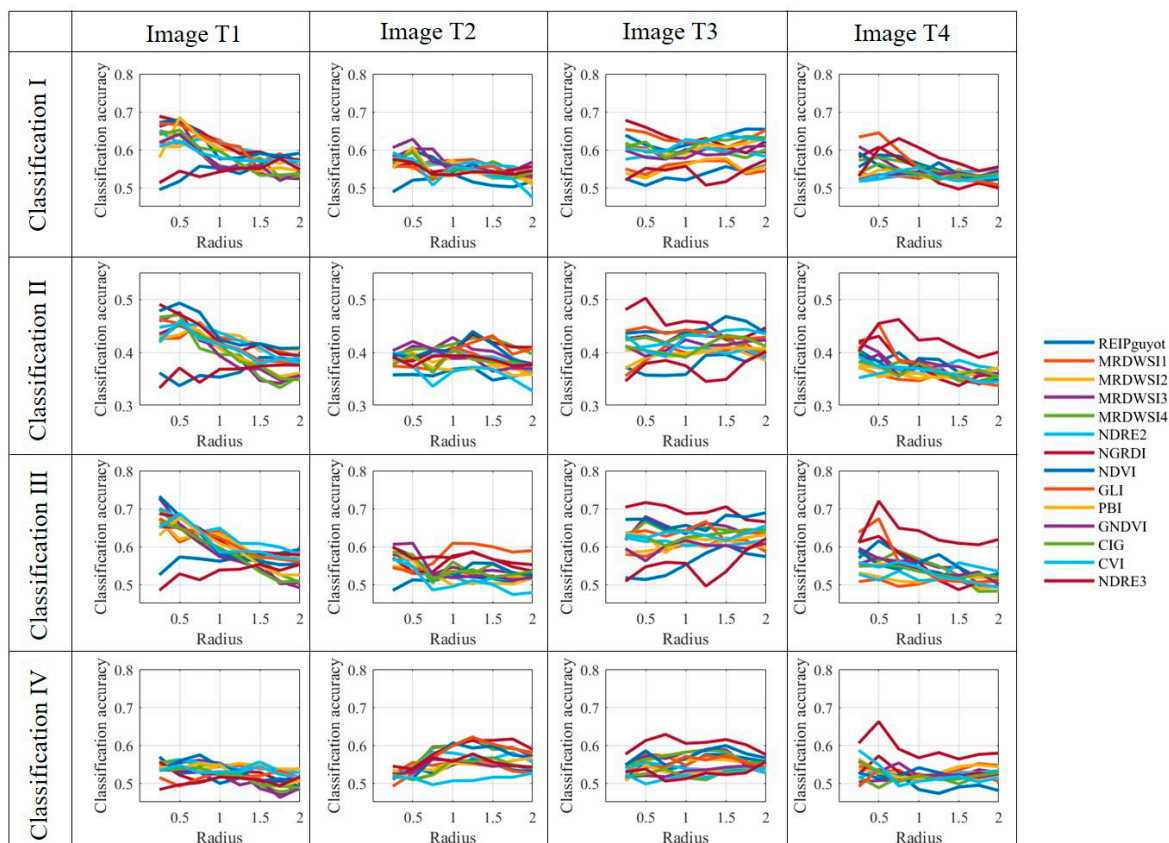


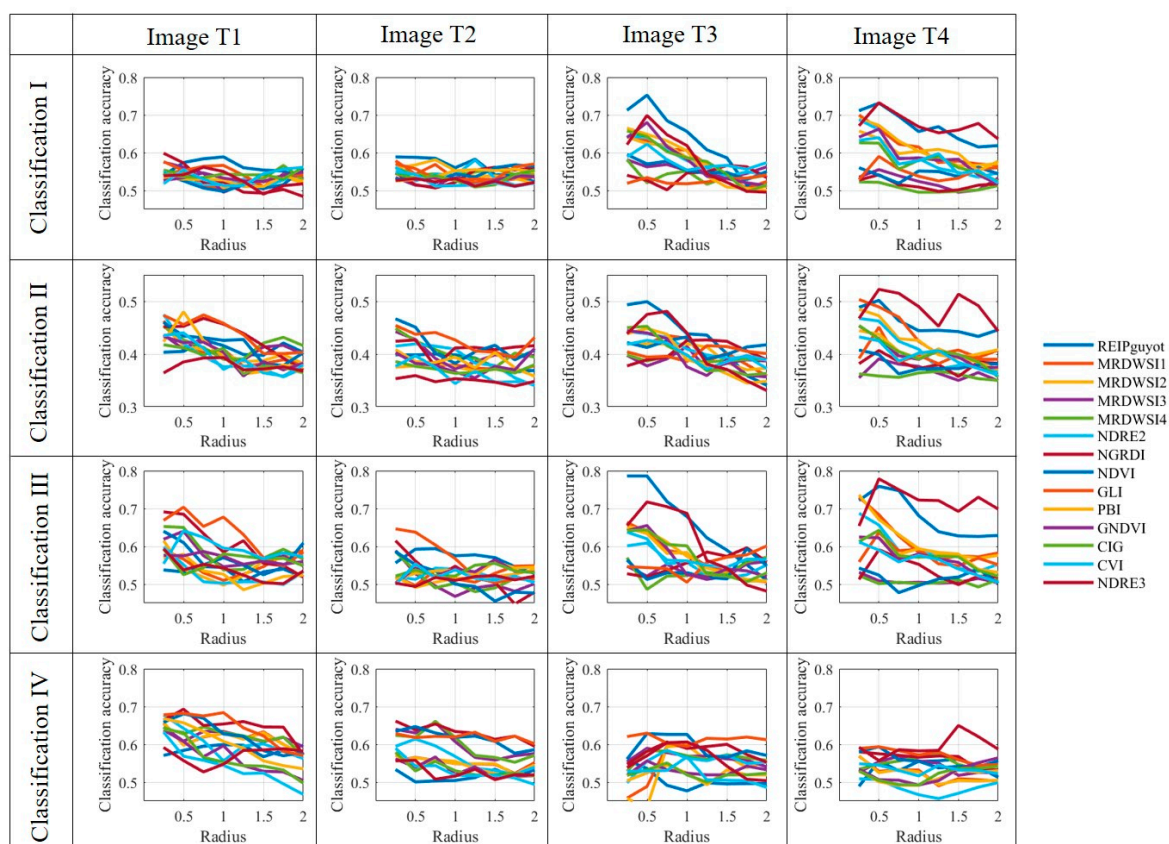
Figure 7. Spectral signatures of tree groups in Stand 1 (a1,a2) and Stand 2 (b1,b2) from four different images. (a1,b1) show spectral signatures of healthy and infected trees, and (a2,b2) show spectral signatures of infected trees with >75% needle retention and <75% needle retention.

3.3. Effective Radius of the Segmentation

The effective radius was first studied by comparing the classification accuracy when using different crown radii from the tree segments. The accuracy between 0.25 and 0.5 m radii was similar, while most VIs in most images decreased when the radius was increased from 0.5 to 2 m (Figure 8). We used 0.5 m as the radius in the following analysis. Note that the accuracy of different VIs in Figure 8 was insufficient to evaluate the classification, as more detailed analyses were needed and presented in the following sections.



(a)



(b)

Figure 8. The obtained separability when using different radii on the tree segments to average the reflectance in Stands 1 (a) and 2 (b).

3.4. Effective VIs and the Distribution

In Stand 1, the classification accuracy was higher when using Images T1 and T3 (Table 6). Using VIs including MRDWSI3, NGRDI, NDVI, GLI obtained higher accuracy than using other tested ones. The accuracy was higher when classifying Group A (healthy) and Group C (severely defoliated trees, needle retention < 75%), while the accuracy was very low with other classification models, implying that VIs could only indicate when trees have severe stress and damage in Stand 1. The highest accuracy was 0.71 using NGRDI on Image T3 to distinguish healthy and severely defoliated trees (Table 6). The distribution of the VIs of different classes also indicated that the severely defoliated trees were more stressed and damaged than the healthy ones (Figure 9a1–a4). However, the δ VIs between images, which can theoretically indicate tree growth within a growing season, showed no stable trend that the healthy group grew more than the infected groups (Figure 9c1–c4).

Table 6. Classification accuracy using different images and different VIs with image radius = 0.5. The relatively high classification accuracy validated with the VIs distribution is highlighted.

Stand No.	VIs	Classification I A vs. B + C			Classification II A vs. B vs. C				Classification III A vs. C				Classification IV B vs. C				
		Image T1	Image T2	Image T3	Image T1	Image T2	Image T3	Image T4	Image T1	Image T2	Image T3	Image T4	Image T1	Image T2	Image T3	Image T4	
1	REIP	0.50	0.54	0.49	0.59	0.34	0.37	0.35	0.39	0.56	0.50	0.51	0.62	0.52	0.56	0.56	0.52
	MR-DSWI1	0.60	0.56	0.53	0.53	0.43	0.40	0.39	0.36	0.61	0.55	0.57	0.52	0.54	0.54	0.57	0.53
	MR-DSWI2	0.62	0.58	0.54	0.54	0.43	0.40	0.40	0.35	0.62	0.56	0.57	0.51	0.54	0.53	0.56	0.53
	MR-DSWI3	0.66	0.62	0.57	0.58	0.46	0.41	0.42	0.38	0.67	0.57	0.67	0.57	0.56	0.54	0.57	0.50
	MR-DSWI4	0.64	0.61	0.61	0.58	0.46	0.42	0.43	0.37	0.64	0.59	0.67	0.56	0.56	0.54	0.57	0.50
	NDRE2	0.64	0.55	0.59	0.51	0.45	0.39	0.40	0.36	0.66	0.55	0.60	0.52	0.57	0.53	0.56	0.53
	NGRDI	0.68	0.58	0.67	0.60	0.47	0.39	0.49	0.43	0.68	0.52	0.71	0.61	0.52	0.54	0.62	0.56
	NDVI	0.67	0.58	0.61	0.56	0.49	0.40	0.44	0.37	0.69	0.58	0.68	0.55	0.56	0.52	0.59	0.51
	GLI	0.66	0.54	0.64	0.64	0.45	0.40	0.45	0.44	0.65	0.52	0.65	0.68	0.49	0.53	0.54	0.53
	PBI	0.64	0.57	0.60	0.55	0.46	0.40	0.41	0.38	0.67	0.57	0.63	0.56	0.54	0.51	0.53	0.52
	GNDVI	0.63	0.61	0.57	0.54	0.44	0.41	0.40	0.41	0.64	0.61	0.56	0.57	0.53	0.53	0.51	0.53
	CIG	0.63	0.59	0.62	0.54	0.45	0.38	0.40	0.38	0.65	0.55	0.63	0.56	0.55	0.52	0.51	0.52
	CVI	0.63	0.57	0.60	0.53	0.45	0.39	0.41	0.36	0.68	0.55	0.62	0.54	0.53	0.51	0.49	0.55
	NDRE3	0.53	0.54	0.55	0.63	0.37	0.37	0.37	0.46	0.54	0.57	0.55	0.71	0.51	0.54	0.54	0.67
2	REIP	0.59	0.59	0.74	0.73	0.42	0.39	0.49	0.51	0.52	0.60	0.78	0.76	0.59	0.51	0.53	0.55
	MR-DSWI1	0.54	0.57	0.63	0.69	0.43	0.39	0.43	0.48	0.57	0.51	0.64	0.67	0.60	0.57	0.47	0.52
	MR-DSWI2	0.51	0.57	0.63	0.67	0.43	0.39	0.43	0.47	0.56	0.51	0.62	0.68	0.60	0.57	0.45	0.52
	MR-DSWI3	0.57	0.51	0.56	0.53	0.44	0.41	0.41	0.38	0.62	0.52	0.52	0.50	0.61	0.63	0.59	0.56
	MR-DSWI4	0.55	0.52	0.54	0.53	0.44	0.42	0.38	0.36	0.65	0.54	0.50	0.52	0.63	0.62	0.58	0.54
	NDRE2	0.53	0.53	0.62	0.66	0.43	0.41	0.42	0.46	0.54	0.52	0.61	0.66	0.64	0.62	0.56	0.51
	NGRDI	0.58	0.53	0.53	0.55	0.43	0.43	0.37	0.43	0.70	0.57	0.52	0.60	0.69	0.63	0.58	0.57
	NDVI	0.53	0.53	0.55	0.53	0.44	0.44	0.41	0.40	0.60	0.55	0.52	0.52	0.68	0.64	0.63	0.59
	GLI	0.57	0.55	0.52	0.57	0.47	0.45	0.38	0.41	0.70	0.63	0.55	0.64	0.69	0.62	0.63	0.59
	PBI	0.56	0.52	0.66	0.62	0.49	0.37	0.45	0.43	0.60	0.53	0.62	0.62	0.66	0.54	0.52	0.50
	GNDVI	0.53	0.52	0.66	0.62	0.43	0.39	0.45	0.44	0.56	0.54	0.64	0.62	0.61	0.54	0.56	0.51
	CIG	0.53	0.52	0.65	0.64	0.43	0.37	0.44	0.43	0.55	0.54	0.65	0.62	0.63	0.53	0.53	0.51
	CVI	0.54	0.54	0.63	0.63	0.43	0.40	0.42	0.43	0.64	0.56	0.61	0.56	0.57	0.54	0.53	0.55
	NDRE3	0.54	0.52	0.67	0.75	0.37	0.36	0.47	0.52	0.54	0.50	0.70	0.77	0.56	0.56	0.57	0.56

In Stand 2, many VIs indicated that the vitality of Group A (healthy) was lower than that of Group B (needle retention \geq 75%), higher than that of Group C (needle retention < 75%), and higher than that of Group B + C (Figure 9). Therefore, the classification accuracy of Classifications I and II was high if the indication mentioned above was true; otherwise, the classification was based on the wrong assumption. Classifications III and VI still classified Group A as having higher vitality than Group C and Group B as having higher vitality than Group C; therefore, the classification matched with the assumption that healthy trees should have higher vitality than infected trees. Similarly with Stand 1, VIs including MRDWSI3, NGRDI, NDVI, and GLI obtained higher accuracy on Image T1 but not Image T3. Moreover, the accuracy of distinguishing Groups B and C was also relatively high using Image T1, which was followed by Image T2 and T3. Similar to Stand 1, δ VIs in Stand 2 indicated tree growth throughout the season, but there was no clear trend that the healthy ones grew more than the infected ones (Figure 9d1–d4).

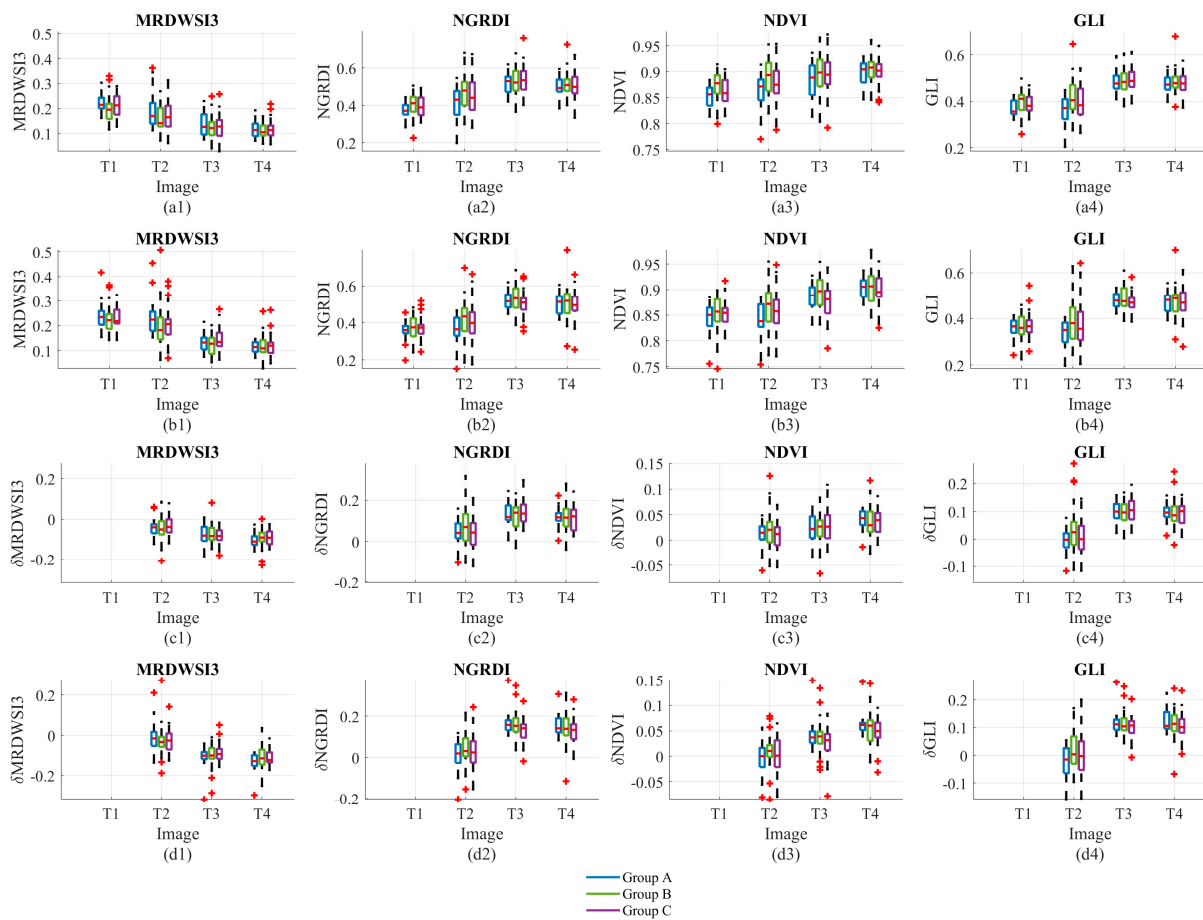


Figure 9. Distribution of VIs of Groups A, B, and C in Stand 1 (a1–a4) and Stand 2 (b1–b4), and distribution of δ VIs in Stand 1 (c1–c4) and Stand 2 (d1–d4).

3.5. Regression of Needle Retention

Linear relationships between the four VIs and the needle retention (%) were found when calculating the group average (Figure 10). In Stand 1, the correlation between group foliage and group average VIs was very strong in Images T1 and T3, e.g., R^2 of 0.99 when using NGRDI in Image T3 (Figure 10a). However, the linear relationship was not as strong for Stand 2 when including tree groups with all levels of defoliation. The VIs indicated that the vitality of the group with 62.5% needle retention was always lower than the group with 87.5% needle retention with all VIs and in all images. However, the tree group with 75% needle retention was an outlier in many images, and the vitality of healthy trees was lower on average than the group with 87.5% needle retention in all images.

Although the linear relationships between the VIs and needle retention were clear at the group level, the inner-group variation was very large, resulting in low accuracy in distinguishing healthy and infected trees or infected trees with different defoliation levels at the individual tree scale. The study did not find a clear trend in the seasonal effect, as the accuracy on Stand 1 was similar when using images from June and September, and the accuracy on Stand 2 was higher when using the image from June. Rather than a seasonal effect, the light condition of the image influenced the estimation more obviously, as Images T3 and T4 were from the same day in September, but the accuracy was higher when using the image with diffused light (T3).

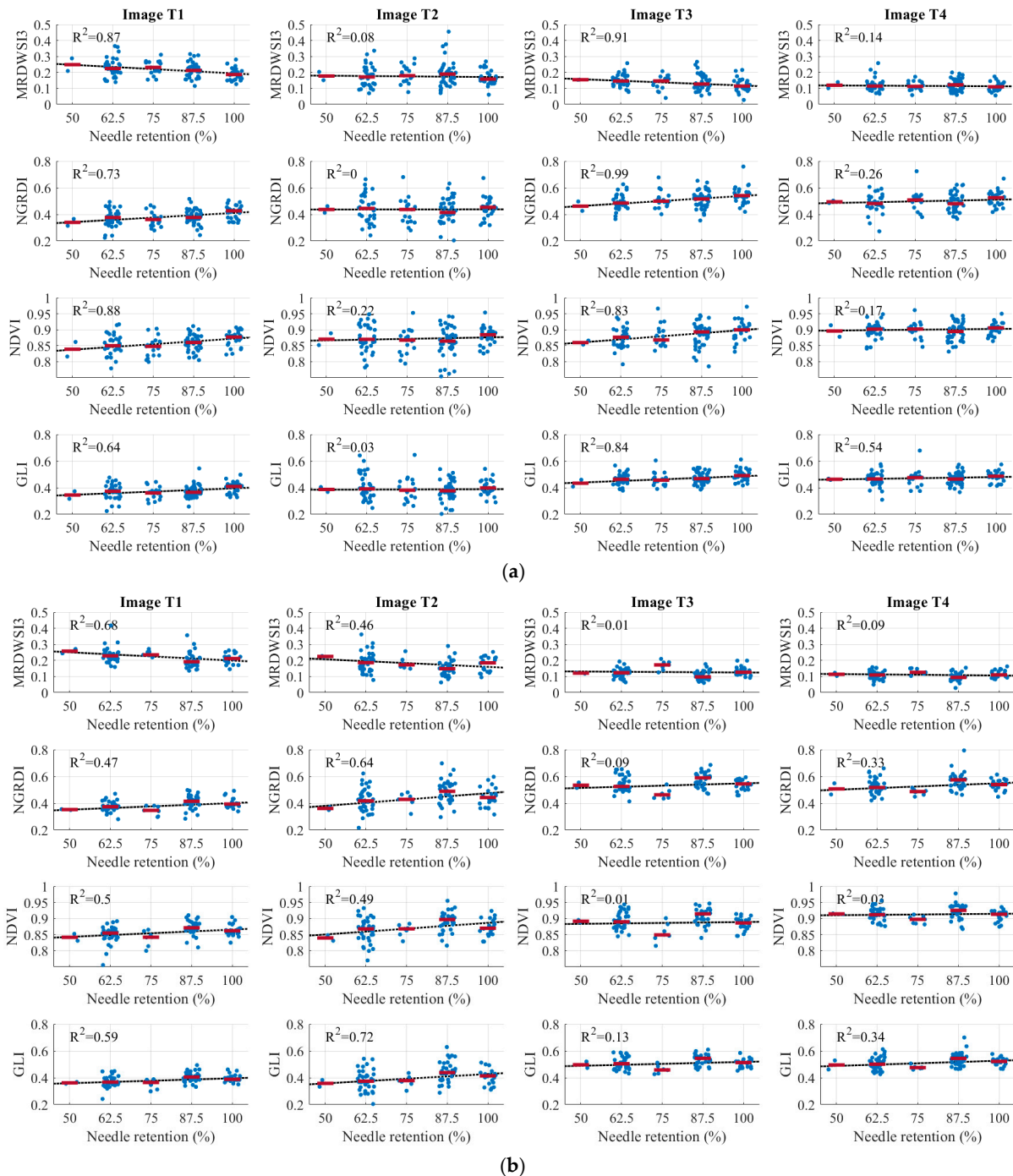


Figure 10. Scatter plots of the VIs of each tree in different needle retention groups and the linear relationship between the group needle retention and average VIs in Stands 1 (a) and 2 (b).

4. Discussion

This study explored how well UAV-based multispectral images could be used to estimate tree vitality decline caused by pine needle pathogens and how well the spectral features obtained from the UAV images matched the visual interpretation of the disease from the ground. Unlike many other studies on detecting acute stress that later led to rapid mortality, this study investigated the detection of trees under chronic stress with minor symptoms. According to the field inventory, almost half of the infected trees had only 12.5% needle loss, and most of the other half had 25–37.5% defoliation. Such minor symptoms made it challenging to estimate the infection level accurately from ground or UAV images.

This challenge was shown from two perspectives in this study. First, this study calculated many VIs shown in previous studies to positively correlate with leaf mass and chlorophyll content. However, those VIs are known to have saturation effects, i.e., stop increasing the values with increasing leaf mass when it comes to large values. The saturation effect could explain the better accuracy in distinguishing healthy trees and trees that lost more than 25% of their needles but were not sensitive to smaller needle retention changes. The low ability to identify trees with mild chronic stress using UAV-based multispectral images was also demonstrated in a study on ash dieback trees infected by *Hymenoscyphus fraxineus*. Although 100% user accuracy was obtained for the class with 50–80% dieback, the classification results showed large confusion between classes with less damage with a kappa coefficient of 0.34 for five-class classification (0, 0–5%, 5–20%, 20–50%, 50–80%). Even when classifying trees with damage levels below and above 5%, the accuracy was unsatisfactory (kappa coefficient of 0.67). The same data and classification methods were used to classify healthy trees and trees infested with spruce bark beetle *Ips typographus*, and the classification accuracy was much higher (kappa coefficient of 0.73), highlighting that it was more challenging to identify trees with mild damage under chronic stress than acute stress [34].

Second, determining the needle retention level for each tree was challenging during the fieldwork and could lead to bias in reference data. The trees in the study were mature and 15–20 m tall, so it was difficult to see through tree crowns and visually estimate the defoliation on the upper part of the crown. The bias was more pronounced in Stand 2, where trees were bigger and taller than trees in Stand 1 (average height of 18.8 m vs. 15.1 m). The VIs showed that some trees were stressed, and symptoms of discoloration of some trees could be seen from the UAV images (Figure A1). However, the symptoms could not be seen from the ground and thus were inventoried as healthy trees. This result underscores the importance of UAV imagery, as it can assist in the (early) detection and monitoring of forest health with the high ability to capture detailed information from the upper tree canopy. Our results showed a strong correlation between group-averaged VIs and needle retention in Stand 1, indicating VIs could be good indicators of the damage level. Using the same VIs for Stand 2 might result in a better estimation of the damage level than the visual estimation from the field. Although the identification accuracy of around 0.70 obtained in this study might not be satisfactory for monitoring purposes, it was relatively high compared to other studies on chronic diseases. For example, a study used a UAV-based camera to investigate the identification of spruce health issues associated with stem damage caused by mechanical means or biotic (*Armillaria ostoyae*) factors. The study found a significant difference ($p < 0.05$) in NDVI between healthy trees and trees with mechanical damage and resin exudation, the latter of which is commonly associated with basal lesions caused by *A. ostoyae*. However, the distribution of NDVI shown in the figure had large overlapping values between the healthy and damaged groups, indicating poor classification accuracy when separating the two groups [35]. Another study used a UAV-based thermal camera to analyze how the canopy temperature could indicate trees with red band needle blight disease caused by the fungus *Dothistroma septosporum* on diseased Scots pine. The infection level was estimated from the ground as the proportion of infected to uninfected tree crowns, which was expressed as a percentage of total live crown length. Correlation was found between canopy temperature depression and disease level with R^2 between 0.27 and 0.41 [36]. A study used UAV-based hyperspectral images to classify healthy trees, trees with the root rot pathogen *Heterobasidion annosum*, and trees in the early stage of spruce bark beetle (*I. typographus*) infestation. The model identified 18 out of 28 trees infested by bark beetles, but only 3 out of 16 trees with root rot [20], underscoring the challenges to identifying chronic diseases than acute infection, which was similar to the

findings of [34]. A study used UAV images to detect brown spot needle blight caused by *Lecanosticta acicola* (synonym = *Mycosphaeralla dearnessii*), and the detection accuracy was 59–67% for diseased trees, although deep learning models were used [32]. High accuracy was only obtained in a study using close-range sensing (UAV images from 7–15 m altitude) to estimate the disease severity of spruce infected by the needle rust pathogen *Chrysomyxa rhododendri*, which can cause defoliation, reduced tree growth and hinder regeneration. A significant linear correlation between the disease severity and image analysis characteristics was found with an R^2 of 0.98 [33].

This study also explored factors that might affect the identification, e.g., images acquired from different seasons, different light conditions, and crown reflectance calculation. The results from the spectral analysis demonstrated no seasonal trend of disease development or decline in tree vitality during one growing season, as evidenced by (1) the spectral separability of healthy and infected groups, which did not increase by the end of the season, and (2) the fact that many VIs still increased in value from June to September, indicating all trees, even the infected ones, still grew and increased leaf mass and chlorophyll content (Figure 9b1–b4,c1–c4). When a tree is severely infected and suffers massive defoliation, water relations are altered and photosynthetic activity is reduced, consequently slowing tree growth [36]. However, the infected trees in this study did not show a trend of slowing down growth compared to the healthy ones, as indicated by the δ VIs (Figure 9b1–b4,c1–c4). The study highlighted the differences in detecting trees under acute and chronic stress. Trees under acute stress, such as European bark beetle infestation and pine wilt disease caused by the pine wood nematode (*Bursaphelenchus xylophilus*), usually show seasonal effects that are easy to detect declining trees late in the season but challenging at the early stage [21,37–39]. In contrast, trees exhibiting chronic stress like those in our study could be detected throughout the season.

Nevertheless, different classification accuracies appeared using different images T1 to T4, which was probably due to the tree phenology and light conditions of the images. The detection was better using images T1 (June 30), when trees started growing new needles, and T3 (September 23), when the old needles naturally dropped off. While image T2 was acquired on August 31, the foliage of both healthy and infected pine trees was still growing, making it more challenging to identify defoliation covered by new needles. Images T3 and T4 were acquired on September 23 but with different light conditions. Under sunny conditions, more radiance from the ground covered by cast needles could be captured by the camera, thus affecting the classification. The results showed better classification when using the centermost pixels in the crown than using entire crowns. Although branches at the crown edges might provide more discolored needles for better classification, the crown edges were also more likely to be affected by the ground radiance than crown centers. These results are consistent with another study that found centermost pixels more efficient for early detection than entire tree crowns [40].

This study also highlighted the importance of developing explainable classification models than ‘black box’ models. Without evaluating the VIs distribution and disqualifying classifications that indicated healthy trees being more damaged than infected trees, the study would have given a very high accuracy, close to 0.8, which can be very misleading. Many machine learning and deep learning models, such as Random Forest, Support Vector Machine, and Convolutional Neural Network, can often be data-driven and train models as black boxes without explainable classification standards. When working with forest stress, especially chronic disease, one should be aware that errors and biases often exist in visual-interpretation-based field data, and using data-driven models may result in misleading conclusions.

This study used multispectral imagery to detect infected trees, yet future studies can explore the potential of hyperspectral imagery, which provides data that are more sensitive to plant photosynthesis activities and physiological changes under stress [17]. In New Zealand, a study used UAV hyperspectral imagery to detect *Dothistroma* needle blight, caused by the fungi *Dothistroma septosporum* and *D. pini*, and the model of disease severity was moderately precise ($R^2 = 0.52$) using narrow-band hyperspectral indices. But the study also found a marked improvement of the model ($R^2 = 0.85$) when adding inverted plant functional traits, highlighting the potential of UAV hyperspectral imagery when developing explainable variables with 3D radiative transfer model [41]. As defoliation was the main symptom of the studied pathogen infection, laser scanning data may be better for the identification without saturation problems than optical data. Some studies have shown an accurate estimation of defoliation caused by pine caterpillar *Dendrolimus tabulaeformis* using terrestrial laser scanning data [42,43]. With the development of UAV-based laser scanning techniques, there is big potential to develop accurate monitoring methods using UAV-based laser scanning data.

5. Conclusions

This study investigated the possibility of detecting pine needle diseases using nine-band multispectral drone images acquired four times across the season and different light conditions. An automatic crown segmentation was carried out with an 89–94% successful rate, and better disease detection was achieved using central pixels in crowns, e.g., <0.5 m radius to the crown center. The best classification model appeared when classifying healthy trees and trees with more than 25% defoliation, and the overall classification accuracy was around 0.70 for different stands and using different VIs. VIs, including MRDWSI3, NGRDI, NDVI, and GLI exhibited higher accuracy and robustness than many other tested VIs. Trees with less than 25% defoliation did not show sufficient separation from healthy trees. When grouping trees with the same needle retention levels, the averaged VIs showed strong correlations (0.73–0.99 of R^2) with the needle retention levels, but the VIs also showed large within-group variance. We did not observe a clear trend of seasonal effects on detectability, but we discovered that light conditions affected detectability significantly. In Stand 2, both visual interpretation and spectral analysis on the drone images confirmed some infected trees that failed to be identified from the ground-based survey. We conclude that using multispectral drone images and implementing the proposed data analysis framework can assist in identifying pine needle diseases in forest health monitoring programs.

Author Contributions: Conceptualization, M.C. and J.B.; Methodology, L.H., I.M., J.B. and M.C.; Software, L.H.; Validation, L.H.; Formal analysis, L.H.; Data curation, L.H.; Writing—original draft, L.H., I.M. and M.C.; Writing—review and editing, L.H., I.M. and M.C.; Visualization, L.H.; Investigation, L.H., I.M. and M.C.; Resources, I.M., J.B. and M.C.; Project administration, M.C.; Funding acquisition, M.C. All authors have read and agreed to the published version of the manuscript.

Funding: This research was funded by the Swedish Research Council Formas, grant # 2018-00966. Data processing was partly funded by the Bröderna Edlunds donationsfond grant # 52957183.

Data Availability Statement: The data presented in this study are available on request from the corresponding author due to privacy.

Acknowledgments: We gratefully acknowledge Kinga Stolarek, Henrik Holmberg, Anders Jakobsson, James Connell, and Anton Holmström for their assistance with the field study.

Conflicts of Interest: The authors declare no conflicts of interest.

Appendix A

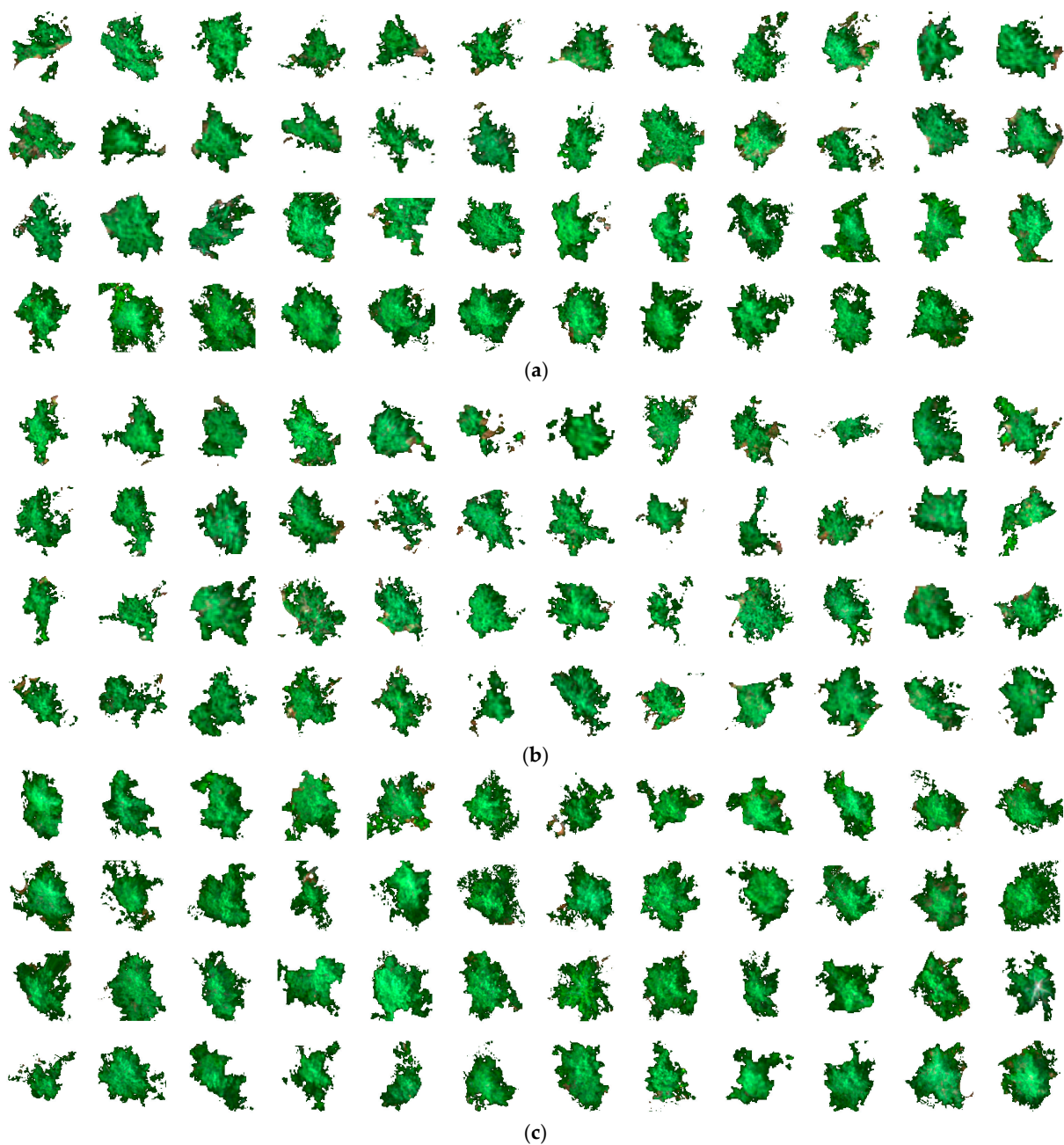


Figure A1. Tree crown segments of healthy trees (a), examples of infected trees from Stand 1 (b) and Stand 2 (c).

References

1. Salmon, Y.; Torres-Ruiz, J.M.; Poyatos, R.; Martinez-Vilalta, J.; Meir, P.; Cochard, H.; Mencuccini, M. Balancing the risks of hydraulic failure and carbon starvation: A twig scale analysis in declining Scots pine. *Plant Cell Environ.* **2015**, *38*, 2575–2588. [[CrossRef](#)] [[PubMed](#)]
2. Allen, C.D.; Macalady, A.K.; Chenchouni, H.; Bachelet, D.; McDowell, N.; Vennetier, M.; Kitzberger, T.; Rigling, A.; Breshears, D.D.; Hogg, E.H.; et al. A global overview of drought and heat-induced tree mortality reveals emerging climate change risks for forests. *For. Ecol. Manag.* **2010**, *259*, 660–684. [[CrossRef](#)]
3. Bose, A.K.; Gessler, A.; Bolte, A.; Bottero, A.; Buras, A.; Cailleret, M.; Camarero, J.J.; Haeni, M.; Hereş, A.-M.; Hevia, A.; et al. Growth and resilience responses of Scots pine to extreme droughts across Europe depend on predrought growth conditions. *Glob. Change Biol.* **2020**, *26*, 4521–4537. [[CrossRef](#)]

4. Bogachev, M.I.; Gafurov, A.M.; Iskandirov, P.Y.; Kaplun, D.I.; Kayumov, A.R.; Lyanova, A.I.; Pyko, N.S.; Pyko, S.A.; Safonova, A.N.; Sinitca, A.M.; et al. Reversal in the drought stress response of the Scots pine forest ecosystem: Local soil water regime as a key to improving climate change resilience. *Heliyon* **2023**, *9*, e21574. [[CrossRef](#)]
5. Jalkanen, R. The occurrence and importance of *Lophodermella sulcigena* and *Hendersonia acicola* on Scots pine in Finland. *Karstenia* **1985**, *25*, 53–61. [[CrossRef](#)]
6. Hanso, M.; Drenkhan, R. Lophodermium needle cast, insect defoliation and growth responses of young Scots pines in Estonia. *For. Pathol.* **2012**, *42*, 124–135. [[CrossRef](#)]
7. Millberg, H.; Hopkins, A.J.M.; Boberg, J.; Davydenko, K.; Stenlid, J. Disease development of *Dothistroma* needle blight in seedlings of *Pinus sylvestris* and *Pinus contorta* under Nordic conditions. *For. Pathol.* **2016**, *46*, 515–521. [[CrossRef](#)]
8. Ata, J.P.; Burns, K.S.; Stewart, J.E. Needle pathogens of Rhytismataceae: Current knowledge and research opportunities for conifer foliar diseases. *For. Pathol.* **2024**, *54*, e12851. [[CrossRef](#)]
9. Sturrock, R.N.; Frankel, S.J.; Brown, A.V.; Hennon, P.E.; Kliejunas, J.T.; Lewis, K.J.; Worrall, J.J.; Woods, A.J. Climate change and forest diseases. *Plant Pathol.* **2011**, *60*, 133–149. [[CrossRef](#)]
10. Gaylord, M.L.; Kolb, T.E.; Pockman, W.T.; Plaut, J.A.; Yepez, E.A.; Macalady, A.K.; Pangle, R.E.; McDowell, N.G. Drought predisposes piñon-juniper woodlands to insect attacks and mortality. *New Phytol.* **2013**, *198*, 567–578. [[CrossRef](#)]
11. Oliva, J.; Stenlid, J.; Martínez-Vilalta, J. The effect of fungal pathogens on the water and carbon economy of trees: Implications for drought-induced mortality. *New Phytol.* **2014**, *203*, 1028–1035. [[CrossRef](#)] [[PubMed](#)]
12. Jurc, D.; Jurc, M.; Sieber, T.N.; Bojovic, S. Endophytic *Cenangium ferruginosum* (Ascomycota) as a Reservoir for an Epidemic of *Cenangium Dieback* in Austrian Pine. *Phyton Ann. Rei Bot. Horn* **2000**, *40*, 103–108.
13. Ryu, M.; Mishra, R.C.; Jeon, J.; Lee, S.K.; Bae, H. Drought-induced susceptibility for *Cenangium ferruginosum* leads to progression of *Cenangium-dieback* disease in *Pinus koraiensis*. *Sci. Rep.* **2018**, *8*, 16368. [[CrossRef](#)] [[PubMed](#)]
14. Ecke, S.; Dempewolf, J.; Frey, J.; Schwaller, A.; Endres, E.; Klemmt, H.-J.; Tiede, D.; Seifert, T. UAV-Based Forest Health Monitoring: A Systematic Review. *Remote Sens.* **2022**, *14*, 3205. [[CrossRef](#)]
15. Hernández-Clemente, R.; Navarro-Cerrillo, R.M.; Suárez, L.; Morales, F.; Zarco-Tejada, P.J. Assessing structural effects on PRI for stress detection in conifer forests. *Remote Sens. Environ.* **2011**, *115*, 2360–2375. [[CrossRef](#)]
16. Ecke, S.; Stehr, F.; Frey, J.; Tiede, D.; Dempewolf, J.; Klemmt, H.-J.; Endres, E.; Seifert, T. Towards operational UAV-based forest health monitoring: Species identification and crown condition assessment by means of deep learning. *Comput. Electron. Agric.* **2024**, *219*, 108785. [[CrossRef](#)]
17. Huo, L.; Koivumäki, N.; Oliveira, R.A.; Hakala, T.; Markelin, L.; Näsi, R.; Suomalainen, J.; Polvivaara, A.; Junttila, S.; Honkavaara, E. Bark beetle pre-emergence detection using multi-temporal hyperspectral drone images: Green shoulder indices can indicate subtle tree vitality decline. *ISPRS J. Photogramm. Remote Sens.* **2024**, *216*, 200–216. [[CrossRef](#)]
18. Luo, Y.; Huang, H.; Roques, A. Early Monitoring of Forest Wood-Boring Pests with Remote Sensing. *Annu. Rev. Entomol.* **2022**, *68*, 277–298. [[CrossRef](#)]
19. Li, N.; Huo, L.; Zhang, X. Using only the red-edge bands is sufficient to detect tree stress: A case study on the early detection of PWD using hyperspectral drone images. *Comput. Electron. Agric.* **2024**, *217*, 108665. [[CrossRef](#)]
20. Honkavaara, E.; Näsi, R.; Oliveira, R.; Viljanen, N.; Suomalainen, J.; Khoramshahi, E.; Hakala, T.; Nevalainen, O.; Markelin, L.; Vuorinen, M.; et al. Using Multitemporal Hyper- and Multispectral UAV imaging For Detecting Bark Beetle Infestation on Norway Spruce. *Int. Arch. Photogramm. Remote Sens. Spat. Inf. Sci.* **2020**, *XLIII-B3-2020*, 429–434. [[CrossRef](#)]
21. Huo, L.; Lindberg, E.; Bohlin, J.; Persson, H.J. Assessing the detectability of European spruce bark beetle green attack in multispectral drone images with high spatial- and temporal resolutions. *Remote Sens. Environ.* **2023**, *287*, 113484. [[CrossRef](#)]
22. Huo, L.; Persson, H.J.; Bohlin, J.; Lindberg, E. Green Attack or Overfitting? Comparing Machine-Learning- and Vegetation-Index-Based Methods to Early Detect European Spruce Bark Beetle Attacks Using Multispectral Drone Images. In Proceedings of the IGARSS 2023—2023 IEEE International Geoscience and Remote Sensing Symposium, Pasadena, CA, USA, 16–21 July 2023; IEEE: New York, NY, USA, 2023; pp. 546–549, ISBN 979-8-3503-2010-7.
23. Huo, L.; Yu, R.; Lindberg, E.; Persson, H.J.; Bohlin, J.; Li, N. Influence of Crown Pixel Selection on the Early Detection of Bark Beetle Infestations Using Multispectral Drone Images. In Proceedings of the IGARSS 2024—2024 IEEE International Geoscience and Remote Sensing Symposium, Athens, Greece, 7–12 July 2024; IEEE: New York, NY, USA, 2024; pp. 5218–5221, ISBN 979-8-3503-6032-5.
24. Guyot, G.; Baret, F.; Major, D.J. High spectral resolution: Determination of spectral shifts between the red and the near infrared. *Int. Arch. Photogramm. Remote Sens.* **1988**, *11*, 750–760.
25. Barnes, E.M.; Clarke, T.R.; Richards, S.E.; Colaizzi, P.D.; Haberland, J.; Kostrzewski, M.; Waller, P.; Choi, C.; Riley, E.; Thompson, T.; et al. (Eds.) Coincident Detection of Crop Water Stress, Nitrogen Status, and Canopy Density Using Ground-Based Multispectral Data. In Proceedings of the 5th International Conference on Precision Agriculture, Bloomington, IN, USA, 16–19 July 2000.
26. Tucker, C.J. Red and photographic infrared linear combinations for monitoring vegetation. *Remote Sens. Environ.* **1979**, *8*, 127–150. [[CrossRef](#)]

27. Rouse, J.; Haas, R.; Schell, J.; Deering, D. Monitoring Vegetation Systems in the Great Plains with ERTS. *NASA Spec. Publ.* **1974**, *351*, 309.
28. Louhaichi, M.; Borman, M.M.; Johnson, D.E. Spatially Located Platform and Aerial Photography for Documentation of Grazing Impacts on Wheat. *Geocarto Int.* **2001**, *16*, 65–70. [[CrossRef](#)]
29. Abdullah, H.; Skidmore, A.K.; Darvishzadeh, R.; Heurich, M. Timing of red-edge and shortwave infrared reflectance critical for early stress detection induced by bark beetle (*Ips typographus*, L.) attack. *Int. J. Appl. Earth Obs. Geoinf.* **2019**, *82*, 101900. [[CrossRef](#)]
30. Gitelson, A.A.; Merzlyak, M.N. Remote sensing of chlorophyll concentration in higher plant leaves. *Adv. Space Res.* **1998**, *22*, 689–692. [[CrossRef](#)]
31. Gitelson, A.A.; Gritz, Y.; Merzlyak, M.N. Relationships between leaf chlorophyll content and spectral reflectance and algorithms for non-destructive chlorophyll assessment in higher plant leaves. *J. Plant Physiol.* **2003**, *160*, 271–282. [[CrossRef](#)]
32. Hunt, E.R.; Daughtry, C.S.T.; Eitel, J.U.H.; Long, D.S. Remote Sensing Leaf Chlorophyll Content Using a Visible Band Index. *Agron. J.* **2011**, *103*, 1090–1099. [[CrossRef](#)]
33. Navarro, G.; Caballero, I.; Silva, G.; Parra, P.-C.; Vázquez, Á.; Caldeira, R. Evaluation of forest fire on Madeira Island using Sentinel-2A MSI imagery. *Int. J. Appl. Earth Obs. Geoinf.* **2017**, *58*, 97–106. [[CrossRef](#)]
34. Kampen, M.; Lederbauer, S.; Mund, J.-P.; Immitzer, M. UAV-Based Multispectral Data for Tree Species Classification and Tree Vitality Analysis. In Proceedings of the Dreiländertagung der DGPF, der OVG und der SGPF, Vienna, Austria, 20–22 February 2019.
35. Brovkina, O.; Cienciala, E.; Surov, P.; Janata, P. Unmanned aerial vehicles (UAV) for assessment of qualitative classification of Norway spruce in temperate forest stands. *Geo-Spat. Inf. Sci.* **2018**, *21*, 12–20. [[CrossRef](#)]
36. Smigaj, M.; Gaulton, R.; Suárez, J.C.; Barr, S.L. Canopy temperature from an Unmanned Aerial Vehicle as an indicator of tree stress associated with red band needle blight severity. *For. Ecol. Manag.* **2019**, *433*, 699–708. [[CrossRef](#)]
37. Yu, R.; Huo, L.; Huang, H.; Yuan, Y.; Gao, B.; Liu, Y.; Yu, L.; Li, H.; Yang, L.; Ren, L.; et al. Early detection of pine wilt disease tree candidates using time-series of spectral signatures. *Front. Plant Sci.* **2022**, *13*, 48. [[CrossRef](#)]
38. Li, N.; Zhang, X.; Huo, L. Identifying Nematode-Induced Wilt Using Hyperspectral Drone Images and Assessing the Potential of Early Detection. In Proceedings of the IGARSS 2022–2022 IEEE International Geoscience and Remote Sensing Symposium, Kuala Lumpur, Malaysia, 17–22 July 2022; IEEE: New York, NY, USA, 2022; pp. 512–515, ISBN 978-1-6654-2792-0.
39. Li, N.; Huo, L.; Zhang, X. Exploring Common Hyperspectral Features of Early-Stage Pine Wilt Disease at Different Scales, for Different Pine Species, and at Different Regions. In Proceedings of the IGARSS 2023–2023 IEEE International Geoscience and Remote Sensing Symposium, Pasadena, CA, USA, 16–21 July 2023; IEEE: New York, NY, USA, 2023; pp. 7575–7578, ISBN 979-8-3503-2010-7.
40. Huo, L.; Lindberg, E.; Fransson, J.E.S.; Persson, H.J. Comparing Spectral Differences Between Healthy and Early Infested Spruce Forests Caused by Bark Beetle Attacks using Satellite Images. In Proceedings of the IGARSS 2022–2022 IEEE International Geoscience and Remote Sensing Symposium, Kuala Lumpur, Malaysia, 17–22 July 2022; IEEE: New York, NY, USA, 2022; pp. 7709–7712, ISBN 978-1-6654-2792-0.
41. Watt, M.S.; Poblete, T.; de Silva, D.; Estarija, H.J.C.; Hartley, R.J.L.; Leonardo, E.M.C.; Massam, P.; Buddenbaum, H.; Zarco-Tejada, P.J. Prediction of the severity of Dothistroma needle blight in radiata pine using plant based traits and narrow band indices derived from UAV hyperspectral imagery. *Agric. For. Meteorol.* **2023**, *330*, 109294. [[CrossRef](#)]
42. Huo, L.; Zhang, N.; Zhang, X.; Wu, Y. Tree defoliation classification based on point distribution features derived from single-scan terrestrial laser scanning data. *Ecol. Indic.* **2019**, *103*, 782–790. [[CrossRef](#)]
43. Huo, L.; Zhang, X. A new method of equiangular sectorial voxelization of single-scan terrestrial laser scanning data and its applications in forest defoliation estimation. *ISPRS J. Photogramm. Remote Sens.* **2019**, *151*, 302–312. [[CrossRef](#)]

Disclaimer/Publisher’s Note: The statements, opinions and data contained in all publications are solely those of the individual author(s) and contributor(s) and not of MDPI and/or the editor(s). MDPI and/or the editor(s) disclaim responsibility for any injury to people or property resulting from any ideas, methods, instructions or products referred to in the content.